

1

2 Antiproton to Proton Flux Ratio with the 3 Alpha Magnetic Spectrometer on the 4 International Space Station

5 Von der Fakultät für Mathematik, Informatik und Naturwissenschaften der RWTH Aachen
6 University zur Erlangung des akademischen Grades eines Doktors der Naturwissenschaften
7 genehmigte Dissertation

vorgelegt von

Sichen Li, M.Sc.

aus
Xi'an

12 Berichter: Univ.-Prof. Dr. rer. nat. Stefan Schael

13 Univ.-Prof. Dr. rer. nat. Christopher Wiebusch

14 Tag der mündlichen Prüfung: 20. Oktober 2022

¹⁵ Diese Dissertation ist auf den Internetseiten der Universitätsbibliothek online verfügbar.

Eidesstattliche Erklärung

17 Sichen Li erklärt hiermit, dass diese Dissertation und die darin dargelegten Inhalte die
18 eigenen sind und selbstständig, als Ergebnis der eigenen originären Forschung, generiert
19 wurden.

20 Hiermit erkläre ich an Eides statt

21 1 Diese Arbeit wurde vollständig oder größtenteils in der Phase als Doktorand dieser
22 Fakultät und Universität angefertigt;

23 2 Sofern irgendein Bestandteil dieser Dissertation zuvor für einen akademischen Ab-
24 schluss oder eine andere Qualifikation an dieser oder einer anderen Institution verwen-
25 det wurde, wurde dies klar angezeigt;

26 3 Wenn immer andere eigene- oder Veröffentlichungen Dritter herangezogen wurden,
27 wurden diese klar benannt;

28 4 Wenn aus anderen eigenen- oder Veröffentlichungen Dritter zitiert wurde, wurde stets
29 die Quelle hierfür angegeben. Diese Dissertation ist vollständig meine eigene Arbeit,
30 mit der Ausnahme solcher Zitate;

31 5 Alle wesentlichen Quellen von Unterstützung wurden benannt;

32 6 Wenn immer ein Teil dieser Dissertation auf der Zusammenarbeit mit anderen basiert,
33 wurde von mir klar gekennzeichnet, was von anderen und was von mir selbst erarbeitet
34 wurde;

35 7 Kein Teil dieser Arbeit wurde vor deren Einreichung veröffentlicht.

36 Aachen, 22. Oktober 2022

Abstract

37

38 Antiproton to Proton Flux Ratio with the Alpha Magnetic Spectrometer on
39 the International Space Station

40 The measurement of cosmic antiproton is a probe to study the source of cosmic rays and
 41 their propagation. Traditional theories of cosmic antiprotons production are interaction
 42 with the interstellar medium. While the precise measurement of cosmic antiprotons in high
 43 rigidity range helps to reveal the sources of it. On the other hand, in the low rigidity range,
 44 all the cosmic rays are affected by the solar wind, including antiprotons. The long-term
 45 effect can be shown by continuously measuring cosmic antiprotons. Due to the low statistics
 46 of antiprotons and the limit on the duration of data taking, this hasn't been done before
 47 the AMS-02 experiment.

48 The AMS-02 collaboration published antiproton result in 2016 with four years collected
49 data, this presented the antiproton to proton flux ratio up to 450 GV. In this thesis, I will
50 present the antiproton to proton flux ratio up to 525 GV with the latest ten years data. This
51 work is an independent work of AMS-02 Physics Report Part *II* published in 2021 which
52 also showed the flux ratio up to 525 GV. Regarding the analysis in the low rigidity range,
53 in this thesis, I will show the antiproton to proton flux ratio with a six Bartels Rotations
54 time resolution (1 Bartels Rotation is exact 27 days).

In this time-dependent flux ratio result, the impact of solar wind can be observed. With the rigidity going up, the variation of flux ratio due to solar wind is weaker. Above 10 GV the impact of solar wind is ignorable. Compared to the electron to positron flux ratio, the antiproton to proton flux ratio shows a different trend below 3 GV. With the rigidity going up, the trends of these two gradually become the same.

CONTENTS

61	1 : INTRODUCTION	1
62	2 : COSMIC RAYS	3
63	2.1 Cosmic Rays	3
64	2.2 Source of cosmic rays	5
65	2.3 Propagation	6
66	2.4 Cosmic antiprotons measurement	9
67	3 : AMS-02 EXPERIMENT	12
68	3.1 Experiment Overview	12
69	3.2 Transition Radiation Detector	14
70	3.3 Silicon Tracker	17
71	3.4 Time Of Flight	20
72	3.5 Ring-Imaging Cherenkov Detector	22
73	3.6 Electromagnetic Calorimeter	23
74	3.7 Anti-Coincidence Counter	24
75	4 : ANALYSIS	26
76	4.1 Data Selection	27
77	4.2 Charge Confusion Estimator	33
78	4.3 TRD Estimator	37
79	4.4 Template Fit	40
80	4.5 Effective Acceptance	48
81	4.6 Measuring Time	52
82	4.7 Trigger Efficiency	59
83	4.8 Unfolding	62
84	4.9 Antiproton To Proton Ratio Calculation	67
85	4.10 Systematic Uncertainty	70
86	5 : RESULTS	75
87	5.1 Time Averaged Result	75
88	5.2 Time Dependent Result	80
89	6 : SUMMARY	90
90	A : APPENDIX - INPUT VARIABLES FOR CHARGE CONFUSION . . .	95

91	B : APPENDIX - YYY	96
92	Acknowledgments	97
93	BIBLIOGRAPHY	98

₉₄ CHAPTER 1

₉₅ INTRODUCTION

₉₆ The story of cosmic rays began in 1912 when a balloon experiment carried out by Victor
₉₇ Hess showed a significant rise in the air ionization rate with increasing altitude, confirming
₉₈ the existence of cosmic rays [1] . The discovery of cosmic rays opened a new window to
₉₉ explore our universe supplementing the astronomical observations. Since then, enormous
₁₀₀ effort has been put in to identify the components of cosmic rays and to measure their flux
₁₀₁ in a wide energy scale range. Due to the very high levels of energy that cosmic rays can
₁₀₂ reach, they provide a unique opportunity to study high energy particles with energy above
₁₀₃ the TeV scale and even higher than the energy levels reached by modern particle colliders.

₁₀₄ Before any particle accelerator was build, the main source to study high energy particles was
₁₀₅ the cosmic rays. The positron was firstly found in 1932 by Carl David Anderson in cosmic
₁₀₆ rays [2] . That was the first antiparticle to be discovered. After that, particle accelerators
₁₀₇ made great progress and the antiproton was discovered in 1955 by Emilio Segrè and Owen
₁₀₈ Chamberlain at the Bevatron particle accelerator [3] . The presence of antiprotons in cosmic
₁₀₉ rays was firstly confirmed in 1979 by two balloon experiments. Give the references of the
₁₁₀ two ballon experiments that confirmed the antiproton in cosmic rays, the effort to study
₁₁₁ cosmic antiprotons has never stopped.

₁₁₂ Due to the Earth's atmosphere, the cosmic antiprotons can only be measured either by
₁₁₃ balloon experiments or space spectrometers. In this thesis, data collected by the AMS-
₁₁₄ 02 experiment is used to determine the antiproton to proton flux ratio, including time
₁₁₅ averaged analysis and time dependent analysis. The AMS-02 detector was installed on the
₁₁₆ International Space Station (ISS) in May 2011 and has a permanent magnet to distinguish
₁₁₇ the sign of the particles' rigidity. Up to May 2021, cosmic ray data of ten years has been
₁₁₈ collected, and is used for the present analysis.

₁₁₉ Before the AMS-02 experiment, there was no continuous measurement of cosmic antipro-
₁₂₀ tons. Some balloon experiments measured cosmic antiprotons in several flights. The Space
₁₂₁ spectrometer PAMELA published only time averaged antiproton results [4] . Since AMS-02
₁₂₂ has been monitoring cosmic rays continuously up to today, the time dependent antiproton
₁₂₃ analysis is possible to be done with the data collected. In this thesis, the time dependent

124 antiproton to proton flux ratio is presented in six Bartels Rotations time resolution (one
125 Bartels Rotation = 27 days), this is the first time that the solar modulation's effect on
126 cosmic antiprotons is shown.

127 Chapter 2 presents a general picture of cosmic rays. An overview of the AMS-02 experiment
128 and its sub-detectors is given in Chapter 3. Chapter 4 describes the antiproton analysis
129 techniques used in this thesis. The result of time averaged antiproton to proton flux ratio
130 using ten years of AMS-02 data, as well as the time dependent antiproton to proton flux
131 ratio with a time resolution of six Bartels Rotations are presented in Chapter 5. Chapter 6
132 gives a summary and a conclusion on this thesis.

₁₃₃ CHAPTER 2

₁₃₄ COSMIC RAYS

₁₃₅ 2.1. Cosmic Rays

₁₃₆ The humankind has been continuously driven by the curiosity to explore the unknown world.
₁₃₇ Up to today the highest particle energy that can be achieved through man-made particle
₁₃₈ accelerators is at the few TeV scale. To study the beyond, our universe itself serves as a
₁₃₉ tool. Universe is the ultimate laboratory for particle physics.

₁₄₀ The spectrum of cosmic rays covers an incredibly wide range in intensity and energy. The
₁₄₁ measured cosmic ray flux is seen at Earth varying about 31 orders of magnitude, which
₁₄₂ corresponds to the scale of the visible Universe compared to the human hair diameter. The
₁₄₃ measured energy of cosmic rays can go up to the ZeV level (10^{21} eV), such an unprecedented
₁₄₄ energy can not be currently generated by man-made facilities. The large dynamic range can
₁₄₅ be seen in figure 2.1(a). As shown in this figure, the cosmic ray flux follows a power law:
₁₄₆ $J(E) \propto E^{(-\gamma)}$ with a spectral index $\gamma \approx 2.7$. Below 10^{10} eV (10 GeV) the flux is lower than
₁₄₇ the power law extrapolation due to the deflection caused by the solar magnetic field. From
₁₄₈ around 3×10^{15} (3 PeV) to 4×10^{18} eV (4 EeV), the spectrum index steeps to around 3.1,
₁₄₉ which is called "knee". Above 4 EeV the spectrum index backs to around 2.7, the transition
₁₅₀ period is called "ankle". In addition, although the theoretical upper limit on the energy
₁₅₁ of cosmic ray protons, the Greisen–Zatsepin–Kuzmin (GZK) limit, is equal to 5×10^{19} eV
₁₅₂ (50 EeV) [5, 6], there are experiments, which appear to have detected cosmic rays with
₁₅₃ energies higher than this limit [7, 8]. This fact poses an unsolved puzzle that needs to be
₁₅₄ investigated. These features and observations are important to understand the sources of
₁₅₅ cosmic rays and their propagation.

₁₅₆ Earth is constantly bombarded by subatomic particles. Due to the Earth's atmosphere, the
₁₅₇ ground based cosmic rays experiments can only measure cascades of cosmic rays. To measure
₁₅₈ the cosmic rays directly, detectors have to be placed above the atmosphere. The AMS-02
₁₅₉ experiment is conducted on the ISS, which maintains an orbit with an average altitude of
₁₆₀ 417 km, therefore it can precisely measure the cosmic rays avoiding their interactions with
₁₆₁ the atmosphere.

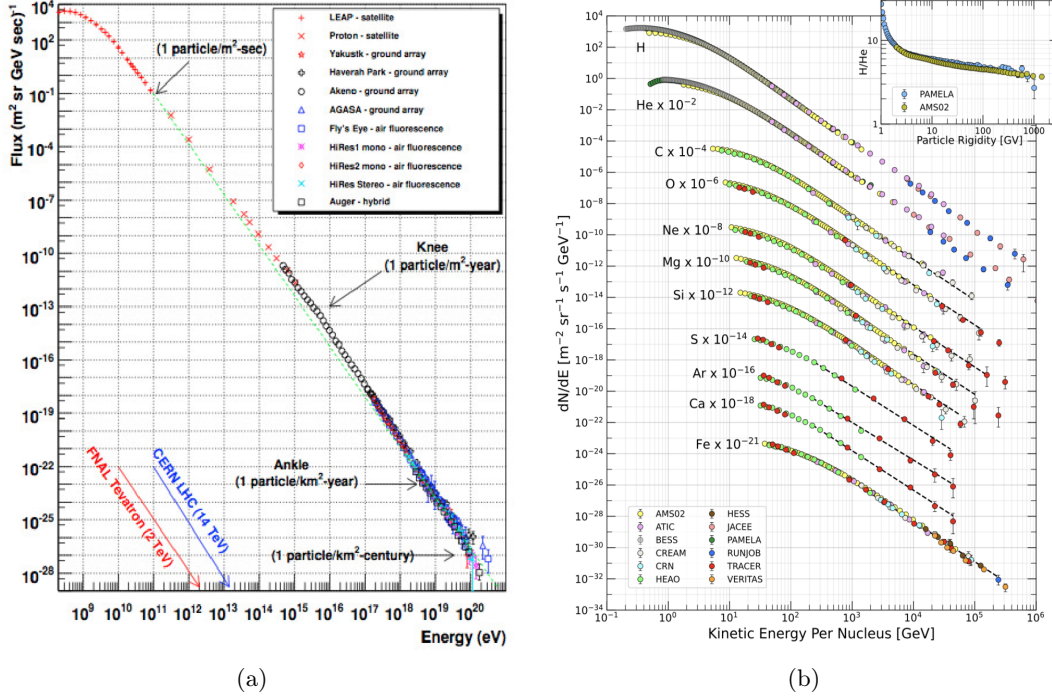


Figure 2.1: (a). Cosmic ray spectrum has a wide range in flux and energy [9], the knee is at around 1 PeV and the ankle is at 4 EeV. (b). The fluxes of different components of cosmic rays follow a universal power law trend [10].

162 There are two kinds of cosmic rays: primary and secondary. Primary cosmic rays are
 163 produced in astrophysical sources, while the secondary cosmic rays are produced from the
 164 interactions between the primary cosmic rays and the interstellar medium. Primary cosmic
 165 rays mainly comprise protons, electrons and He, while secondary cosmic rays consist of
 166 mainly positrons, antiprotons, Li, Be, B, and others.

167 Cosmic rays consist of many components. For primary cosmic rays, 89% are protons, 10%
 168 are helium nuclei and around 1% are heavy elements. In figure 2.1(b) the fluxes of different
 169 cosmic ray components are shown. A universal power law spectrum is observed in all kinds
 170 of cosmic rays, which supports the assumption of a general electro-magnetic acceleration
 171 mechanism, though small differences are still need to be investigated. With the efforts of
 172 different measurements, the fluxes of cosmic ray components have been measured for a large
 173 energy range.

174 In figure 2.2, the abundances of the galactic cosmic rays (GCR) arriving near Earth compared
 175 to the ones of the solar system are shown. In general, there is good agreement between
 176 these two kinds of abundances. The reduced abundance of the galactic cosmic hydrogen and
 177 helium is due to the effects of the solar magnetic field. Due to the spallation and interactions
 178 of the cosmic rays, the C, N and O nuclei would break into elements of lower mass, namely

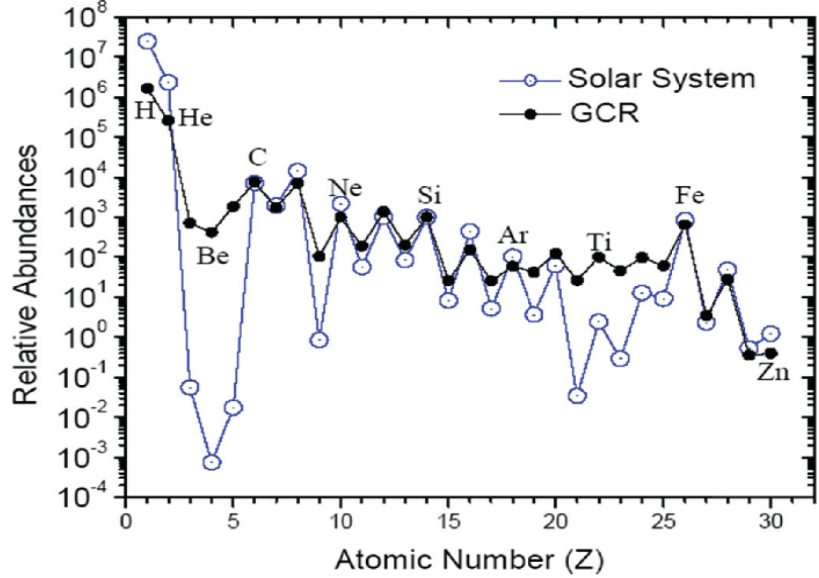


Figure 2.2: A good agreement of element abundances between the GCR and the solar system is shown [11] , except some differences like over-abundance of H and He in solar system, excess of Li, Be, B in GCR and others.

179 Li, Be, and B. This fact explains the higher abundances of Li, Be and B in the GCR.

180 **2.2. Source of cosmic rays**

181 Traditionally, the supernova remnants (SNRs) are considered to be the main source of cosmic
 182 rays. This idea was firstly suggested by Baade and Zwicky in 1934 [12] . Apart from
 183 SNR, some other sources can also contribute to cosmic rays production, like pulsars or dark
 184 matter. Therefore, a high precision measurement of the cosmic ray flux is certainly a probe
 185 to understand the sources of cosmic rays.

186 The supernova is a stellar explosion event that can expel several solar masses of material
 187 with very high speed. There are mainly two mechanisms of supernova creation [13] : a) a
 188 white dwarf reaches the Chandrasekhar mass limit and a nuclear fusion is triggered, and b)
 189 a massive star undergoes gravitational core collapse. During a supernova explosion, matter
 190 is ejected and accelerated at velocities of a few percent of the speed of light. As the ejected
 191 material travels faster than the speed of sound in the ISM it creates an expanding shock wave
 192 that sweeps up the interstellar material of gas and dust creating a "supernova remnant" [14]
 193 .

194 Charged particles can be absorbed into the supernova remnant and be confined in it. They
 195 gain energy and are accelerated while trapped in the supernova remnant until their energy is
 196 large enough to escape from it. The acceleration mechanisms are called "First Order Fermi
 197 Mechanism" and "Second Order Fermi Mechanism". The first one describes the particles

198 crossing the shock front repeatedly gaining energy [15] . The second one describes the
 199 acceleration from the particle collisions with magnetic clouds in the interstellar medium [16]
 200 . These acceleration processes in the supernova remnant would eventually lead to a power
 201 law energy spectrum.

202 Apart from the SNRs, pulsars can also produce high energy cosmic rays. Pulsars are rapidly
 203 rotating neutron stars with strong magnetic field. A pulsar wind nebula (PWN) is usually
 204 formed around a pulsar within the shell of a supernova remnant, where electrons and
 205 positrons can be produced by pair production [17, 18] . The shock of the PWN with the
 206 surrounding matter can accelerate, through centrifugal acceleration, these charged particles
 207 to very high energies [19, 20] . This effect results in an important contribution to the cosmic
 208 electron and positron spectra in the high energy range.

209 Pulsars can produce positrons while antiprotons can not be produced by pulsars [21, 22]
 210 . Therefore, the contribution of cosmic antiprotons to the cosmic ray spectrum, can only
 211 result from the interactions between the primary cosmic rays and the ISM. If an excess in the
 212 cosmic antiproton component is ever observed, different sources of antiproton production,
 213 like dark matter should be investigated [23, 24, 25] . Therefore by measuring the antiproton
 214 spectrum precisely, the sources of cosmic antiprotons can be studied.

215 2.3. Propagation

216 2.3.1. Cosmic rays propagating in the galaxy

217 When the accelerated cosmic rays leave the SNR, they would travel through the Galaxy
 218 and then interact with the ISM producing secondary cosmic rays. By hadronic production,
 219 antiprotons can be generated. Positrons and electrons lose their energy by bremsstrahlung.
 220 Due to their charge, cosmic rays are scattered on the magneto-hydrodynamic (MHD) waves,
 221 so their trajectory is deflected from a straight line. The path of cosmic rays can be described
 222 by a diffusion process. The effects of this diffusion, as well as other physical effects can be
 223 quantitatively described by the transport equation [26] :

$$\frac{\partial \psi(\vec{r}, p, t)}{\partial t} = q(\vec{r}, p, t) + \vec{\nabla} \cdot (D_{xx} \vec{\nabla} \psi - \vec{V} \psi) + \frac{\partial}{\partial p} p^2 D_{pp} \frac{\partial}{\partial p} \frac{1}{p^2} \psi - \frac{\partial}{\partial p} \left[\dot{p} \psi - \frac{p}{3} (\vec{\nabla} \cdot \vec{V}) \psi \right] - \frac{1}{\tau_f} \psi - \frac{1}{\tau_r} \psi \quad (2.1)$$

224 where $\psi(\vec{r}, p, t)$ is the density of cosmic rays at point \vec{r} with momentum p . The terms of the
 225 equation describe different physical processes and are explained here:

- 226 • $q(\vec{r}, p, t)$ denotes the source term, that includes the primary sources, and the contributions
 227 from spallation and decay processes.
- 228 • D_{xx} is the spatial diffusion coefficient that describes the scattering off the magneto-

229 hydrodynamic waves.

230 • \vec{V} is the convection velocity. The galactic winds cause an additional convective trans-
231 port and this can lead to adiabatic energy losses.

232 • D_{pp} is the momentum diffusion coefficient. Apart from the spatial diffusion process,
233 charged particles traveling in MHD waves undergo stochastic re-acceleration that can
234 be described by the momentum diffusion coefficient.

235 • $\vec{\nabla} \cdot \vec{V}$ denotes the adiabatic momentum change, this term is caused by scattering off
236 inhomogeneities of the magnetic field.

237 • τ_f and τ_r are the time scales of fragmentation and decay respectively.

238 For each particle type a propagation equation is used, leading to a very complex system of
239 differential equations. To solve these equations analytically is very hard, therefore numerical
240 calculations are more practical, like Monte-Carlo based approaches. Software numerical
241 tools that are widely used to obtain the solution of the transport equation are the following:
242 GALPROP [27] , USINE [28] , and DRAGON [29] .

243 Alternatively, it is possible to solve simplified approximations of Eq. 2.1. Using the basic
244 assumption that the galaxy is a box where particles can freely propagate while undergoing
245 only elastic scattering. At the edge of box the particles are reflected with a probability
246 $1 - P_{esc}$, the P_{esc} is the probability of escaping to outside of box. As a consequence,
247 the diffusion term can be replaced by escape time τ_{esc} . The transport equation can be
248 simplified as:

$$\frac{\partial \psi(\vec{r}, p, t)}{\partial t} = \psi_0(p) \cdot \delta(t) - \frac{\psi(p, t)}{\tau_{esc}} \quad (2.2)$$

249 where τ_{esc} is escape time which represents the constant escape probability, $\psi_0(p)$ is the
250 injection homogenous source of particles at the time $t=0$. This simplified approximation is
251 called the Leaky-Box model [30] and its solution is:

$$\psi(p, t) = \psi_0(p) \exp\left(-\frac{t}{\tau_{esc}}\right) \quad (2.3)$$

252 2.3.2. Cosmic ray propagating in the heliosphere

253 The sun is continuously ejecting from its upper atmosphere a stream of charged particles
254 when the energy of those particles surpass the escape limit, this form the solar wind [31, 32]
255 . The solar wind plasma drags outwards the solar magnetic field forming the heliospheric
256 magnetic field (HMF) [33] . The charged particles of the solar wind reach speeds of around
257 400 km/s, meaning they are faster than the speed of the magnetosonic wave, therefore they

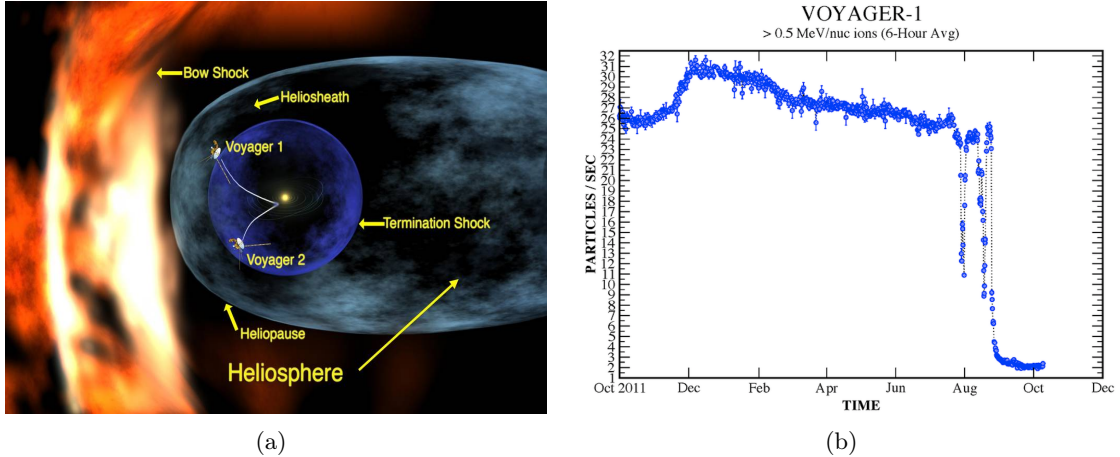


Figure 2.3: a): Diagram of the heliosphere. Credit: NASA/Walt Feimer; b). Particle rate detected by Voyager 1 (from October 2011 through October 2012) [36] .

258 are supersonic. After traveling for some distance and encountering the interstellar medium,
 259 the speed of the solar wind abruptly decelerates and becomes subsonic at the termination
 260 shock [34] . Figure 2.3(a) shows a diagram of the heliosphere. The Voyager 1 probe became
 261 the first spacecraft to cross the termination shock in 2004 and later in 2012 to encounter
 262 the heliopause [35] . As shown in Figure 2.3(b), the solar wind particles rate dramatically
 263 decreases after reaching the outer border of the heliosphere.

264 When galactic cosmic rays enter the solar system, they would travel through the heliosphere
 265 first before reaching Earth. Due to the 22-year cycle of the Sun's activity [37] , and as the
 266 solar wind is emitted from the Sun's corona, the physical status of the heliosphere also varies
 267 following this cycle. After entering the heliosphere, the galactic cosmic rays are modulated
 268 accordingly and therefore they exhibit a variation that follows the solar cycle. The solar
 269 cycles have been counted since 1755 and now we are in solar cycle 25 [38, 39] .

270 In figure 2.4, the different ground based cosmic neutron measurements and the monthly
 271 mean sunspot numbers are shown. Since the sunspot numbers are correlated to the sun
 272 activity, they are anti-correlated with the measured cosmic rays. By measuring the cosmic
 273 ray flux over a long period of time, the impact of the solar activity can be studied. Until
 274 recently, the only continuous cosmic ray flux measurements over a long period of time have
 275 been performed only for the dominant components of the cosmic spectrum like protons,
 276 helium, electron or neutrons produced in cascades in the Earth's atmosphere. There is no
 277 continuous measurement about rare cosmic ray components like the antiproton. Since the
 278 AMS-02 experiment has been collecting cosmic data for 10 years, the first time dependent
 279 antiproton measurement can be achieved.

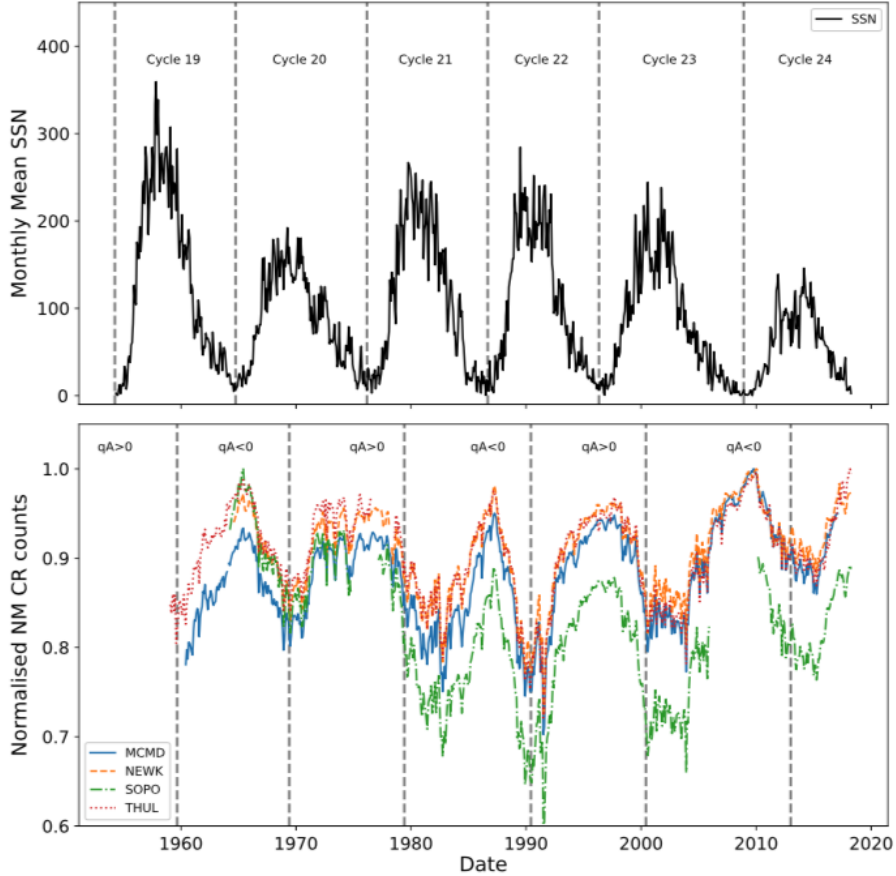


Figure 2.4: Different ground based neutron monitors and monthly mean sunspot numbers in latest six cycles are given in this figure [40] . They show anti-correlated trends.

280 2.4. Cosmic antiprotons measurement

281 Cosmic rays were discovered in 1912 [1] , the antiproton was discovered in 1955 [3] , and the
 282 first measurements of cosmic antiproton component were performed in 1979 [41, 42] , when
 283 two pioneering balloon flight experiments published their results about cosmic antiprotons
 284 independently. The first one was carried out by Bogomolov et al. and the data taking was
 285 from 1972 to 1977 by three individual flights, the residual air was 11 g/cm^2 so a correction
 286 was needed. The result showed two candidates of cosmic antiprotons in the kinetic energy
 287 range of 2-5 GeV.

288 The second one was carried out by R. L. Golden et al. in Palestine in Texas and the data
 289 taking was from June 21 to June 22 1979. The residual air in this area was 5.4 g/cm^2 .
 290 The spectrometer had a superconducting-magnet and the group reported 46 antiproton
 291 candidates from 5.6 to 12.5 GV. In figure 2.5, the cosmic antiproton candidates in those two
 292 experiments are shown.

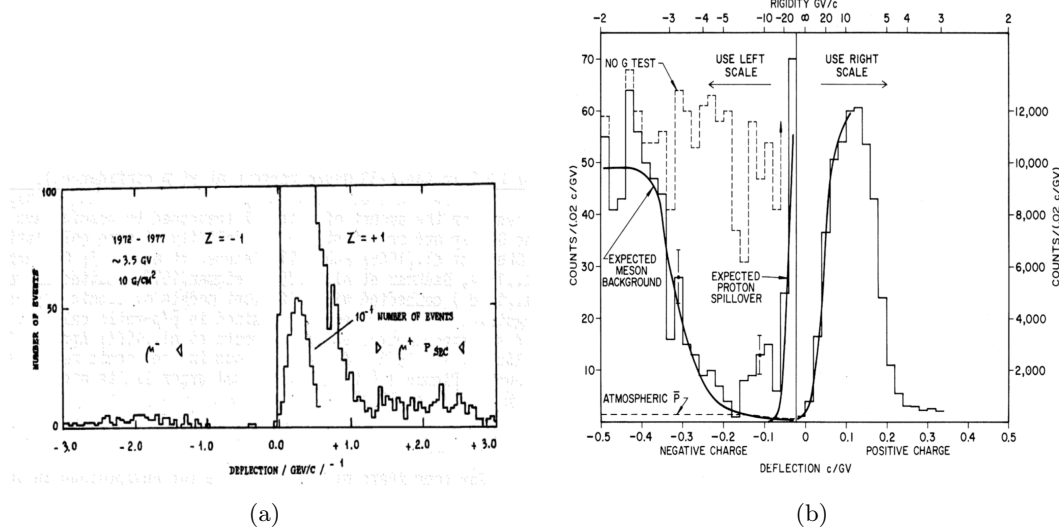


Figure 2.5: a). The antiproton signals in deflection ($1/\text{Rigidity}$) from the balloon flight experiment carried out by Bogomolov et al. in 1979 [41]. b). The antiproton signals in deflection from the balloon flight experiment carried out by Golden et al. in 1979 [42]

- 293 After decades of effort, many cosmic ray experiments published results about cosmic antiprotons.
294 In balloon flight experiments, the representative program is the BESS experiment,
295 which had 9 successful flight campaigns since 1993. The incarnation programs are BESS-
296 Polar I & II [43, 44] carried out in 2004 and 2008 respectively and both flights measured
297 the cosmic antiprotons [45, 46].
- 298 In the final result from BESS-Polar II experiment, the group used data taken from Dec 2007
299 to Jan 2008 (a period corresponding to a solar minimum) and reported the measurement of
300 7886 cosmic antiprotons in the kinetic energy range from 0.17 to 3.5 GeV [46]. Figure 2.6
301 shows the antiproton signals in $1/\beta$ versus Rigidity from BESS-Polar II.
- 302 Due to the limited height of the balloon flight experiments, the correction of the residual air
303 has to be considered to get a flux result above atmosphere. The correction that the residual
304 air creates can be overcome if a spectrometer is placed in space where the residual air is
305 negligible.
- 306 The first satellite based cosmic antiproton measurement was performed by the PAMELA
307 detector. PAMELA's mission lasted from June 2006 to February 2016 at a float altitude
308 between 350 km and 610 km. The orbital period of the host satellite Resurs-DK1 was 94
309 min [47]. The PAMELA group published several antiproton results and the last one was
310 in 2012 [48, 49, 4] with a maximum measured energy of 350 GeV [4]. This result shows
311 a relatively flat antiproton to proton flux ratio in the high energy range, which is different
312 from the traditional prediction of cosmic antiprotons from purely secondary production. In
313 2016 the AMS-02 experiment published its first result on cosmic antiprotons extending the

314 measured rigidity range up to 450 GV using cosmic ray data collected during the first four
 315 years of its operation [50] . The details of AMS-02 experiment will be shown in the next
 316 chapter. The antiproton flux results from these experiments are given in figure 2.7.

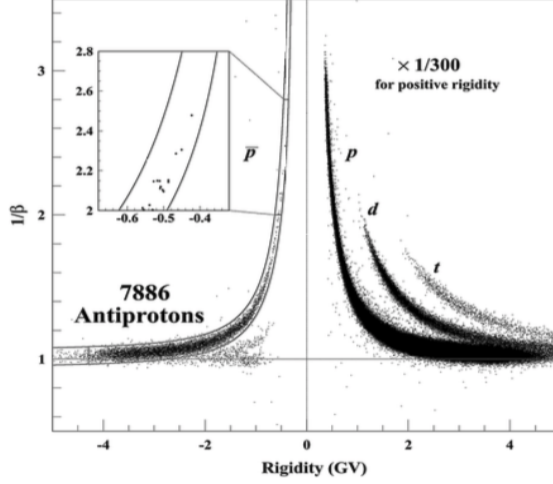


Figure 2.6: The 7886 antiprotons signals and other components measured by BESS-Polar II in $1/\beta$ versus Rigidity [46] .

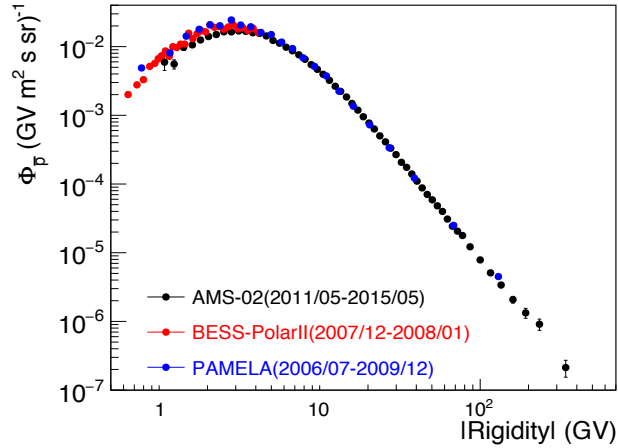


Figure 2.7: The antiproton flux measured by BESS-Polar II, PAMELA, and AMS-02 experiment

317 CHAPTER 3

318 AMS-02 EXPERIMENT

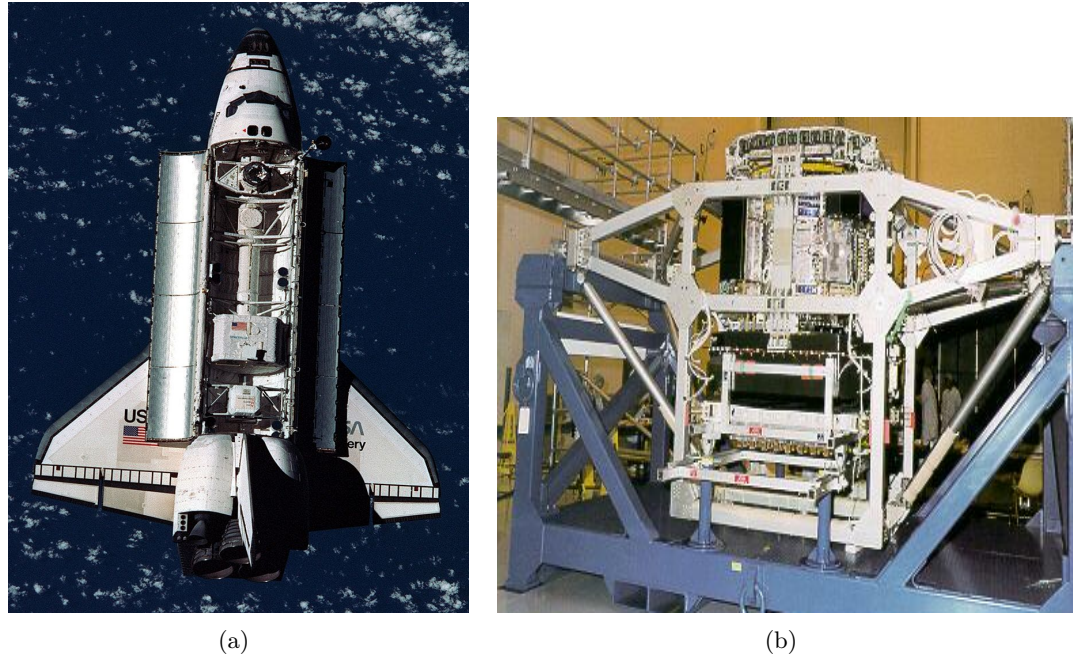
319 3.1. Experiment Overview

320 The Alpha Magnetic Spectrometer (AMS) program was proposed by Nobel Laurent Prof.
321 Samuel Ting from MIT in 1995 and was accepted then [51] . The goal of the experiment
322 is to measure the antimatter in cosmic rays and provide precise measurement of fluxes for
323 different components of cosmic rays, which is crucial to understanding the sources of cosmic
324 rays and the basic propagation model of cosmic rays. [52]

325 To test the feasibility of the particle spectrometer in space, a prototype called AMS-01 was
326 designed, a simplified version of the final experiment, see the detector in figure 3.1(b). The
327 test flight was conducted in 1998 in space shuttle flight STS-91 [53] , see figure 3.1(a). By
328 collecting cosmic rays data for ten days, the test flight proved that putting a spectrometer
329 in space is possible.

330 After several years of construction and testing, the AMS-02 detectors were launched by
331 space shuttle Endeavour in STS 134 mission from Kennedy Space Center on 16 May 2011.
332 Three days later, the detectors were installed on ISS's upper Payload Attach Point (S3) and
333 began data taking. Figure 3.2 shows the location of AMS-02 on the ISS.

334 The AMS-02 experiment has a size of $5 \text{ m} \times 4 \text{ m} \times 3 \text{ m}$, weight of 7.5 t [56] . It has a
335 permanent magnet with 0.14 T, combined with nine silicon tracker layers, the rigidity of
336 the particle can be measured. Within the magnet, the Anti-Coincidence Counters (ACC)
337 are used as a veto system to reject particles from the side. At the relative top of the
338 experiment, there is a Transition Radiation Detector (TRD), which can distinguish light
339 and heavy particles. Above and below the magnet are two Time-Of-Flight (TOF) systems
340 installed to provide the trigger and the measurements of velocity and charge. Below the lower
341 part of TOF, a Ring-Imaging Cherenkov (RICH) detector is located so the particle's velocity
342 can be measured. At the bottom of the detector, there is an Electromagnetic Calorimeter
343 (ECAL) which can measure the energy of particles. The geometry of all the sub-detectors
344 is illustrated in figure 3.3.



(a)

(b)

Figure 3.1: a). AMS-01 test flight aboard Space Shuttle Discovery on the STS-91 mission in June 1998 [54] ; b). AMS-01 detector was installed in the support structure at Kennedy Space Center (NASA). credit: AMS-01 brochure



Figure 3.2: AMS-02 detector mounted on the ISS S3 Upper Inboard Payload Attach Site. Image modified from [55]

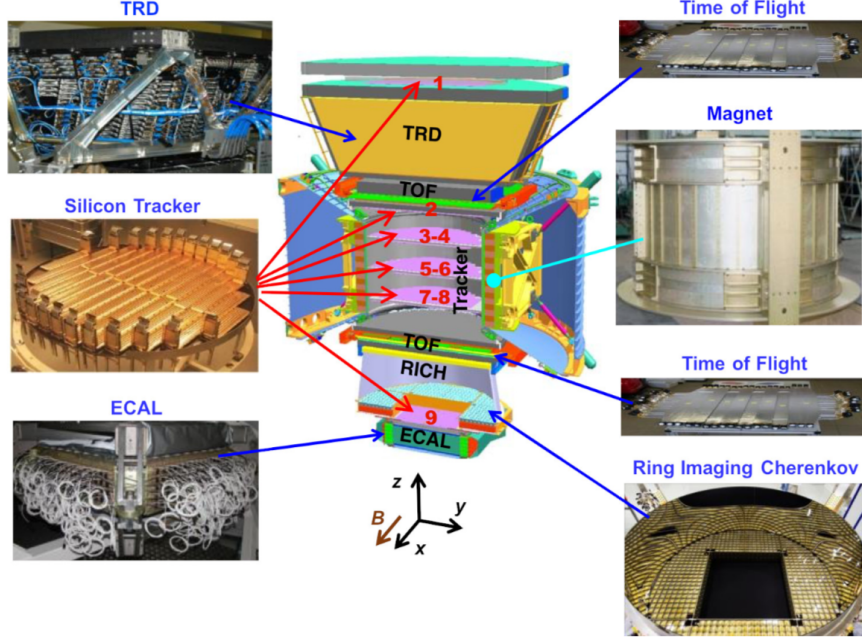


Figure 3.3: Schematic view of AMS-02 experiment and its all sub-detectors. [57]

345 The experiment operations have been conducted since the launch to make the experiment
 346 run smoothly. The operations can be split into flight and underground parts. In figure 3.4
 347 the operation process is illustrated. The collected data is transmitted from upper left to
 348 lower left in this figure with a clockwise sequence. The command from underground to the
 349 space station follows the counterclockwise sequence.

350 3.2. Transition Radiation Detector

351 The TRD can separate different particles by transition radiations. Transition radiation is
 352 emitted when a charged particle goes through the boundary between two different media
 353 [59]. The emitted radiation is produced because of the different inhomogeneous solutions of
 354 Maxwell's equation of charged particle in two media. The particle has to emit photons to
 355 compromise the differences. The intensity of emitted photon is proportional to the Lorentz
 356 factor γ , so for the relativistic charged particle, the characteristic energy of the radiation
 357 is X-ray. The direction is mostly forward, and the angle between transition radiation and
 358 particle path is proportional to $1/\gamma$.

359 AMS-02 experiment has a transition radiation detector placed on the top of the experiment
 360 between tracker layer one and the upper TOF layer [60, 61]. The TRD has 5248 proportional
 361 tubes; each one has a 6 mm diameter and a maximum of 2 meters in length. The tubes
 362 have double-layer 72 μm Kapton aluminum foil walls and at the center of the tube is 30
 363 μm tungsten wire. Inside the tubes there are CO₂ and Xe gas mixture supplied from
 364 storage tanks (5 kg CO₂ and 49 kg Xe). When a charged particle goes through the tube,



Figure 3.4: A overview of AMS-02 experiment operations flow in flight and ground [58]

365 it can ionize the Xe atom and create an avalanche of ionization proportional to the charged
 366 particle's energy loss. Then the CO₂ could quench the environment and reset to the initial
 367 state. So far, no detectable leak in the AMS-02 TRD gas system has been observed. Due
 368 to the diffusion, the loss of CO₂ is around 0.47 g/day, and the loss is ignorable for Xe. This
 369 ensures that TRD can stably operate until 2035.

370 These TRD tubes are assembled in 328 modules, and one module has 16 tubes. Furthermore,
 371 all these modules are mounted in 20 layers. Twelve layers are placed along the Y axis in the
 372 middle of TRD, four layers are placed on top, and four layers are on the bottom. In figure
 373 3.5, the actual size of TRD is shown when its construction was completed in Aachen.

374 In figure 3.6, the left figure shows the response when an electron and a proton go through
 375 one TRD layer. The upper part of the layer is a 20 mm fleece radiator, which has 10 μm
 376 polypropylene or polyethylene fibers. The lower part of the layer is straw tubes. When a
 377 relativistic charged particle goes through the radiator, transition radiation may be produced.
 378 For example, the dE/dx signal can be recorded after a proton traverses the layer. While an
 379 electron passes the layer, the transition radiation can also be collected in straw tubes. The
 380 right figure shows the distributions in tube collected energy for 100 GeV protons and 20
 381 GeV electrons as an example. Due to the transition radiation emitted by electrons, around
 382 10 KeV photons are observed.

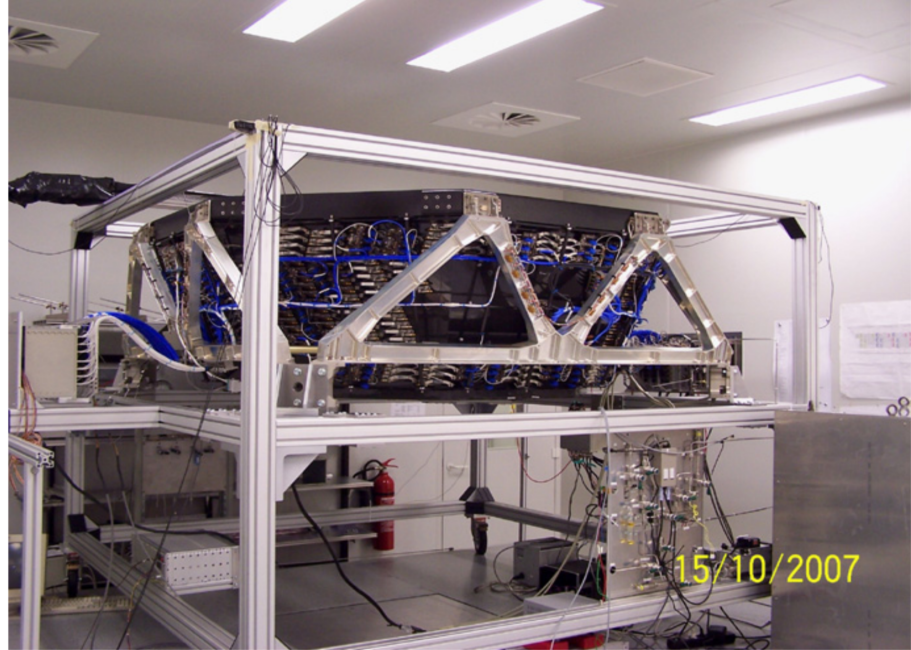


Figure 3.5: TRD final construction completed in RWTH Aachen University. [62]

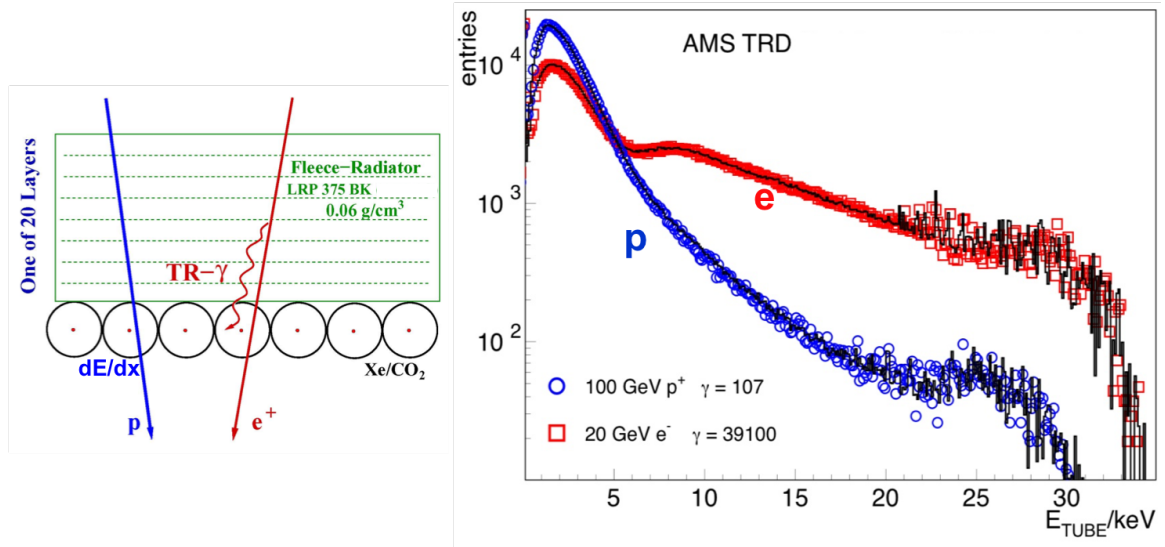


Figure 3.6: Illustration of TRD separation between electrons and protons [58] : the left figure shows the transition radiation emitted by positron while proton only left dEdX signal; the right figure shows an example of tube collected energy for 100 GeV protons and 20 GeV electrons

³⁸³ The signals from the 20 layers are combined to construct a likelihood \mathcal{L} for each particle species. For example, for electron and proton, \mathcal{L}_e and \mathcal{L}_p are constructed. According to

385 Neyman-Pearson lemma [63] , the separation power can reach maximum in the form of the
 386 likelihood ratio. Therefore, the TRD estimator is defined as:

$$\Lambda_{TRD} = -\log\left(\frac{\mathcal{L}_A}{\mathcal{L}_A + \mathcal{L}_B}\right) \quad (3.1)$$

387 If A = electron and B = proton, then the likelihood is "TRDElectronProtonLikelihood"
 388 which provides separation power for electron and proton. In figure 3.7, the distribution of
 389 electron and proton are shown in TRD estimator. The two kinds of particles can be very
 390 well separated, as shown in this figure.

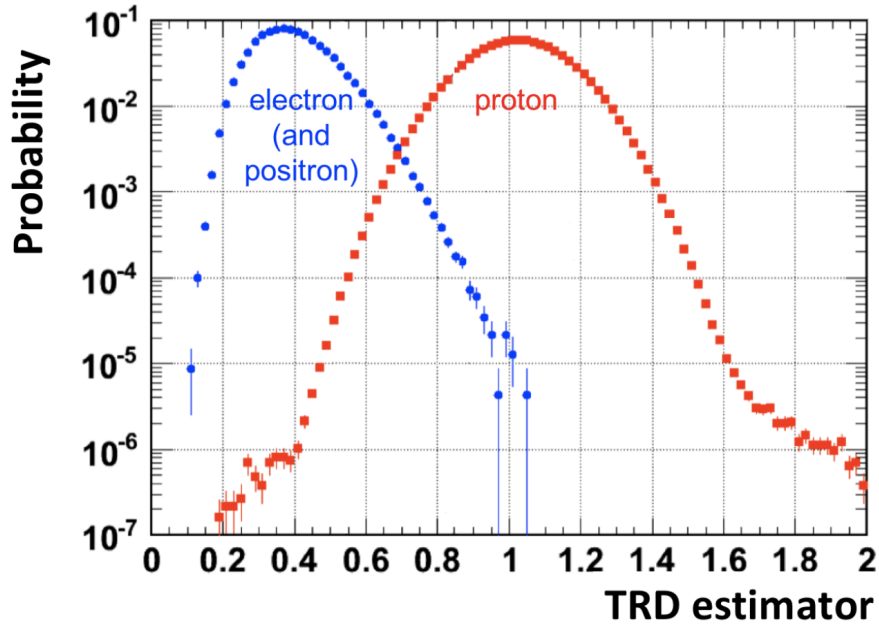


Figure 3.7: Separation between the electrons and protons in TRDLikelihood estimator. [58]

391 3.3. Silicon Tracker

392 To measure the sign of rigidity, a silicon tracker system with a magnet is equipped in the
 393 AMS-02 experiment. Originally the magnet was a superconducting magnet with a 0.8 T
 394 magnetic field [64] . But due to the thermal issue and lifetime of the experiment, the
 395 superconducting magnet was replaced by a permanent magnet [65] . The magnet used in
 396 the AMS-02 experiment is a permanent magnet with a 0.14 T magnetic field. The magnet
 397 has 64 Nd-Fe-B sectors arranged in a cylinder shape with 0.8 m height and 1.1 m diameter
 398 inside. The produced magnetic field is almost linear, and the magnetic field direction is
 399 defined as the X direction, the vertical direction is the Z direction, so the particle bending
 400 plane is the YZ plane. Outside the magnet, the leaking magnetic field is ignorable so that
 401 the design can minimize the magnetic effect on the ISS.

402 In figure 3.8, the permanent magnet used in AMS-02 is shown. Since the magnet is the same
 403 as AMS-01, the magnetic field of the magnet was remeasured again in 2010. Compared with
 404 the first measurement in 1997, the deviation is less than 1% as showed in 3.9.



Figure 3.8: Preparing for the vibration test of the permanent magnet in China Academy of Launch Vehicle Technology (CALT) [58]

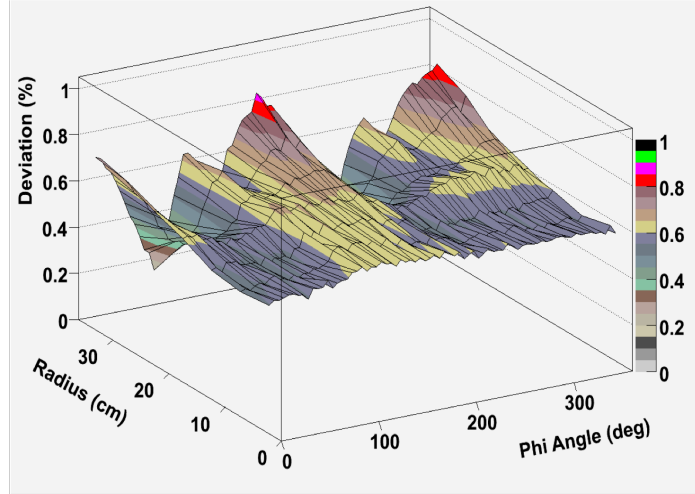


Figure 3.9: Deviation of measured magnetic fields of the permanent magnet between 1997 and 2010 [58] .

- 405 With the permanent magnet, the silicon tracker can measure the charge Z and also the
 406 momentum p of the particle.
 407 The tracker in AMS-02 has nine silicon layers, the first layer is on the top of TRD, the second
 408 layer is above the magnet and below the upper TOF, and layer 3 to 8 are inner central layers
 409 installed inside the permanent magnet, layer 9 is above ECAL and below RICH. In total,
 410 all nine layers have 2264 double-sided silicon micro-strip sensors. They are arranged into

411 192 ladders [66, 67] . The summed-up active measurement area is $6.75 m^2$. Each ladder has
 412 1024 readout strips for signal readout, 640 on the p-side and 384 on the n-side. So in total,
 413 196608 readout strips are reading out the signals.

414 The double-sided silicon micro-strip sensor has size of $41.360 \times 72.045 mm^2 \times 300 \mu m$. A
 415 particle goes through the sensor and creates electron-hole pairs in the middle. The created
 416 electrons would drift toward the n-side and the holes toward the p-side, so both the X and
 417 Y side position measurements are provided. Figure 3.10 illustrate the process. The tracker's
 418 design results in resolutions of $10 \mu m$ and $30 \mu m$ in bending direction and non-bending
 419 direction, respectively. Also, since the signal is proportional to dE/dX measurement, the
 420 charge measurement of each layer can be obtained. The charge resolution of the inner tracker
 421 layers is $\Delta Z = 0.05$ for the charge one particle.

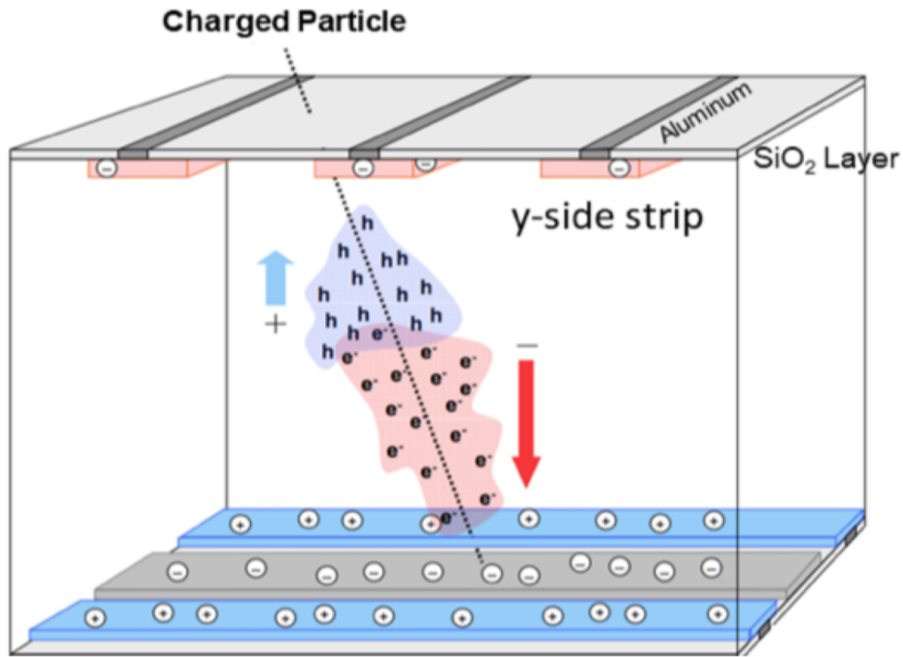


Figure 3.10: Drift of the electron-hole pair in silicon sensor produced by a charged particle.
[\[58\]](#)

422 The inner tracker layer's positions are aligned with 20 IR laser beams with sub-micron
 423 measurement [68, 69] . Layer 1 and 9 position alignments are done with fresh 2 minutes
 424 cosmic rays. This gives $5 \mu m$ and $6 \mu m$ variations for layer 1 and 9, respectively.

425 Before the launch of AMS-02, the whole detector was tested at CERN SPS with proton
 426 beams of 180 and 400 GeV, positron, electron, and pion beams of 10 to 290 GeV. These
 427 extensive calibration data give the precise measurement to determine the tracker rigidity
 428 resolution function and make it possible to compare and calibrate with MC simulation.
 429 Figure 3.11 shows the 400 GeV proton calibration data and MC comparison. A good match
 430 between these two is seen.

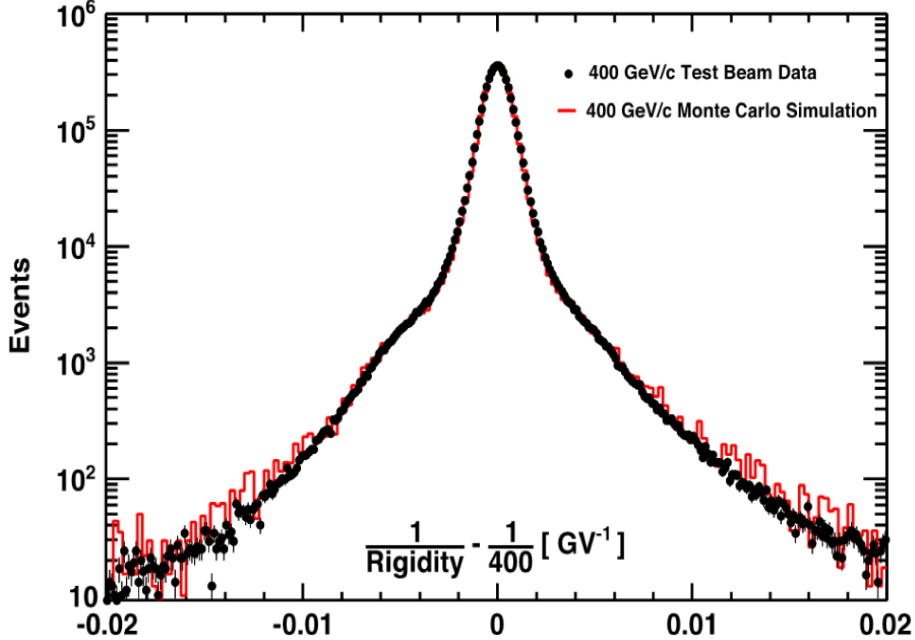


Figure 3.11: Tracker resolution comparison between 400 GeV protons beam test and MC comparison. [58]

431 The electronics and radiators of the tracker produce heat that should be removed by the
 432 tracker thermal cooling system (TTCS). TTCS is a two-phase CO₂ cooling system with four
 433 cooling pumps. Due to the aging and technique problems, the old four pumps were replaced
 434 by four new pumps in several spacewalks from November 2019 to January 2020.

435 3.4. Time Of Flight

436 AMS-02 has four planes of TOF counters, plane 1 and 2 are above the magnet (Upper TOF),
 437 and plane 3 and 4 are below the magnet (Lower TOF) [70, 71]. Plane 1, 2, and 4 have eight
 438 plastic scintillator paddles, while plane 3 has 10. In upper and lower TOF, two planes are
 439 arranged in X and Y directions, respectively, see figure 3.12. To avoid possible gaps between
 440 paddles, the paddles are placed with a 0.5 cm overlapping. Each paddle is also equipped
 441 with 2 or 3 PMTs at the end of the paddle, so the light signal from the plastic scintillator
 442 paddle can be collected by these PMTs and provide efficient detections.

443 Combining the information from all four planes, the TOF system can provide the particle
 444 triggers for the AMS-02 experiment. More details about triggers will be discussed in 4.7.

445 By measuring the ionization energy loss dE/dX, the charge of particles can be independently
 446 obtained from the anode and dynode of PMTs. See figure 3.13(b). The charge resolution is
 447 $\Delta Z = 0.05$ for the charge one particle.

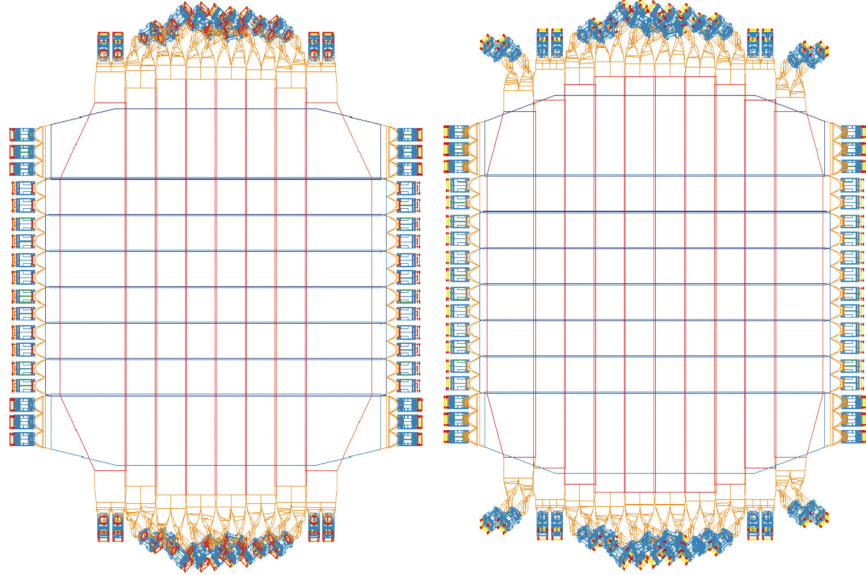


Figure 3.12: TOF planes arrangement in AMS-02 experiment, left is Upper TOF and right is Lower [72] .

448 Except for measuring the charge, TOF can also get the particle's velocity by measuring the
 449 time differences between upper and lower TOF. Each counter's time resolution is around 160
 450 ps, and the combined β resolution is around 4% for $\beta \approx 1$ and $Z = 1$ particles. See figure
 451 3.13(a). This provides the ability to discriminate between the up-going and down-going
 452 particles.

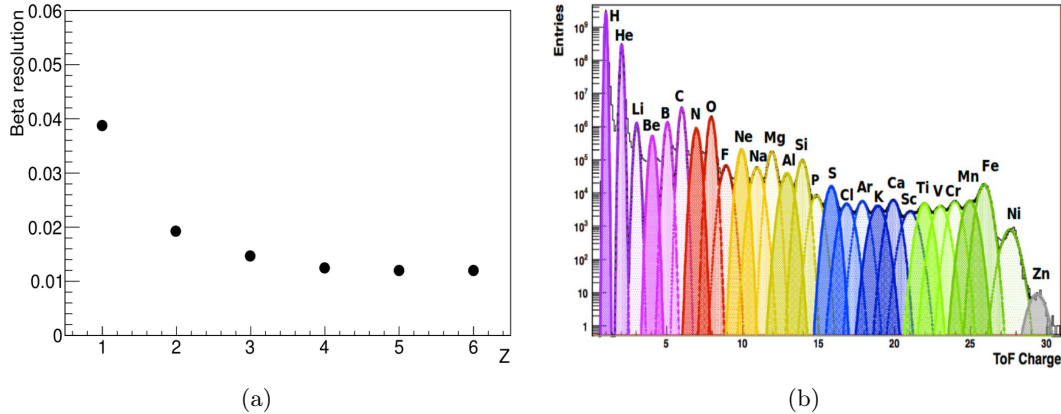


Figure 3.13: a). TOF Beta resolution as the function for particle charge. [72] ; b). TOF charge distribution from proton ($Z=1$) to Zinc ($Z=30$). [72]

453 **3.5. Ring-Imaging Cherenkov Detector**

454 In the AMS-02 experiment, the RICH is installed below the lower TOF and above ECAL.
455 The RICH can measure the velocity and the charge of relativistic particles. The RICH
456 comprises two radiators at the top, an expansion volume in the middle, and a PMT plane
457 at the bottom [73, 74]. See figure 3.14. The whole RICH has the shape of a cone with an
458 upper radius of 60 cm, a lower radius of 67 cm, and a height is 47 cm.

459 When a charged particle traverses a dielectric radiator with a velocity greater than the
460 velocity of light in this material, the particle emits a cone of Cherenkov photons. The RICH
461 in the AMS-02 experiment has a radiator plane of two non-overlapping radiators. The central
462 radiator has 16 sodium fluoride tiles (called NaF) of $85 \times 85 \times 5\text{mm}^3$ with refractive index
463 $n=1.33$. Outside of NaF, there are 92 silica aerogel tiles (called Agl) of $115 \times 115 \times 25\text{mm}^3$
464 with refractive index $n=1.05$ [73].



Figure 3.14: RICH PMT plane and expansion volume in the front and two radiators in the behind. [75]

465 To emit the Cherenkov radiation, the particle's velocity has to surpass the speed of light
466 in the radiator. Since $\beta = v/c$ and $n = c/v$, this leads to the requirement that particles of
467 $\beta > 0.75$ for NaF and particles of $\beta > 0.953$ for Agl can emit radiation.
468 A highly reflective mirror surrounds the expansion volume to increase the detection efficiency.
469 The PMT detection plane is equipped with 680 PMT tubes of 4×4 multi anodes. The
470 effective spatial granularity is $8.5 \times 8.5\text{mm}^2$. The opening angle of the Cherenkov radiation
471 cone $\theta = \arccos(1/n\beta)$.

- 472 The velocity resolution of RICH is $\sigma_\beta/\beta \approx 10^{-3}$ for charge one particle, see figure 3.15(a).
 473 The charge measurement of RICH provides a resolution better than 0.5 for particles of charge
 474 up to 12. See figure 3.15(b) for the resolutions.

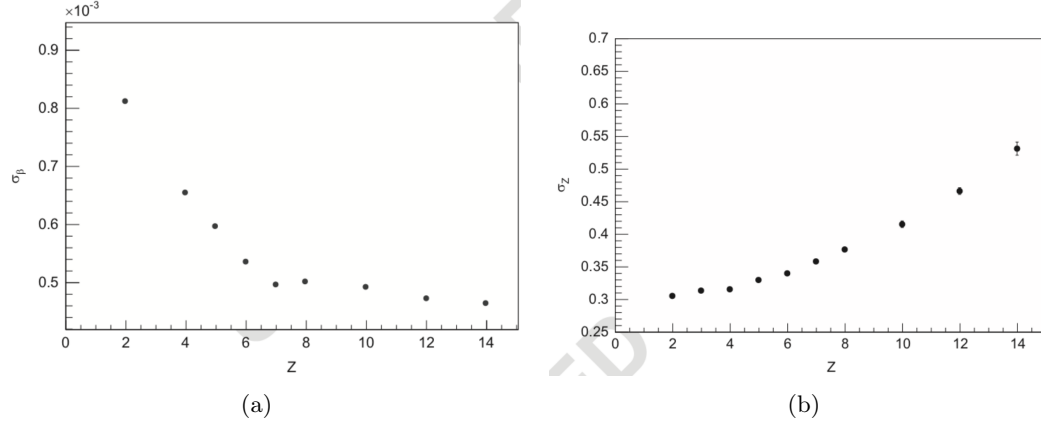


Figure 3.15: a). RICH beta resolution as the function for particle charge. [76] ; b). RICH charge resolution as the function of particle charge. [76]

475 3.6. Electromagnetic Calorimeter

476 The ECAL in the AMS-02 experiment can precisely measure the two profiles of longitude
 477 and latitude of the electromagnetic shower, and the deposited energy [77, 78]. It has a
 478 lead-scintillating fiber sandwich structure with an active area of $648 \times 648\text{mm}^2$, a thickness
 479 of 166mm and a weight of ≈ 500 kg. The ECAL has 98 lead foils and 50000 scintillating
 480 fibers in total. The radiation length is around 17.

481 The ECAL consists of 9 superlayers with a thickness of 18.5 mm. Each superlayer is made
 482 of 11 grooved lead foils alternate with ten fiber layers glued together with optical epoxy
 483 (see figure 3.16) [79], while the last superlayer is made of aluminum. Also, one superlayer
 484 is placed in one direction only. By alternatively stacking the nine superlayers in X and Y
 485 directions, the 3D image of the shower shape is obtained (five in the X direction and four in
 486 the Y direction). Each superlayer is read out by 36 PMTs at only one edge. To avoid dead
 487 zone, the PMTs are arranged alternatively. In total, the ECAL has 324 PMTs, 1296 nodes
 488 [80].

489 When a particle goes through the ECAL, it will interact in an electromagnetic or a hadron-
 490 icdal way to produce a shower [81]. An electromagnet shower comprises electrons and
 491 positrons, while a hadronic shower primarily consists of pions and kaons by interaction or
 492 decay. Therefore the hadronic shower looks wider and more likely to be irregular.

493 The energy resolution has been determined by beam test [82] and can be described by [83]
 494 :

$$\frac{\sigma(E)}{E} = \frac{(10.4 \pm 0.2)\%}{\sqrt{E(\text{GeV})}} \oplus (1.4 \pm 0.1)\% \quad (3.2)$$

495 In figure 3.17, the comparison between measured data and the function is given.

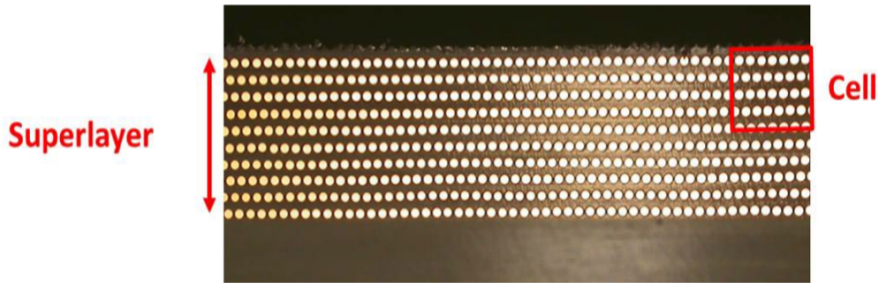


Figure 3.16: ECAL super layer structure and cell dimensions. [80]

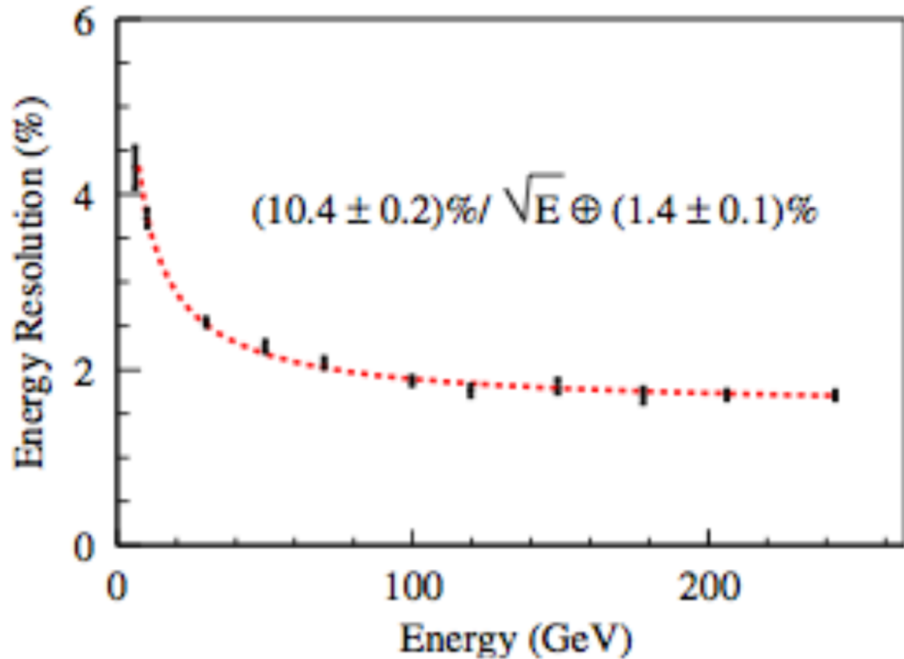


Figure 3.17: ECAL energy resolution from beam test data [83] .

496 **3.7. Anti-Coincidence Counter**

497 The ACC in the AMS-02 experiment is installed surrounding the inner tracker inside the
498 magnet bore [84, 85] , see figure 3.18 upper left one. The first purpose is to reject unwanted
499 events like particles entering AMS-02 from the side or secondary interacting with the sub-
500 detectors. The second task for the ACC is to reduce the trigger rate when the ISS is going

501 through the area overwhelmingly dominant by low energy large flux like SAA [86] .

502 The ACC has a cylinder shape of 1.1 m in diameter and 0.83 m in height. It is composed
503 of 16 scintillator panels (Bicron BC-414) with 8 mm thickness, see the upper right figure
504 in 3.18. When the particles traverse the ACC panels, the particle will emit photons by
505 ionization energy loss in the scintillators. Then the light would be absorbed by the fibers
506 (WLS, Kuraray Y-11(200)M) that are embedded into the panels, and transported to PMTs
507 (Hamamatsu R5946) at the end.

508 A pair of panels are connected to two same PMTs through clear fibers, see figure 3.18 lower
509 one. The design is to have some redundancies and also save weight. The slot between these
510 two panels has a tongue and groove structure to minimize the inefficiency of detections. After
511 integrating sub-detectors in 2008, panels' efficiency is determined at CERN using muons to
512 be 99.99% [58] .

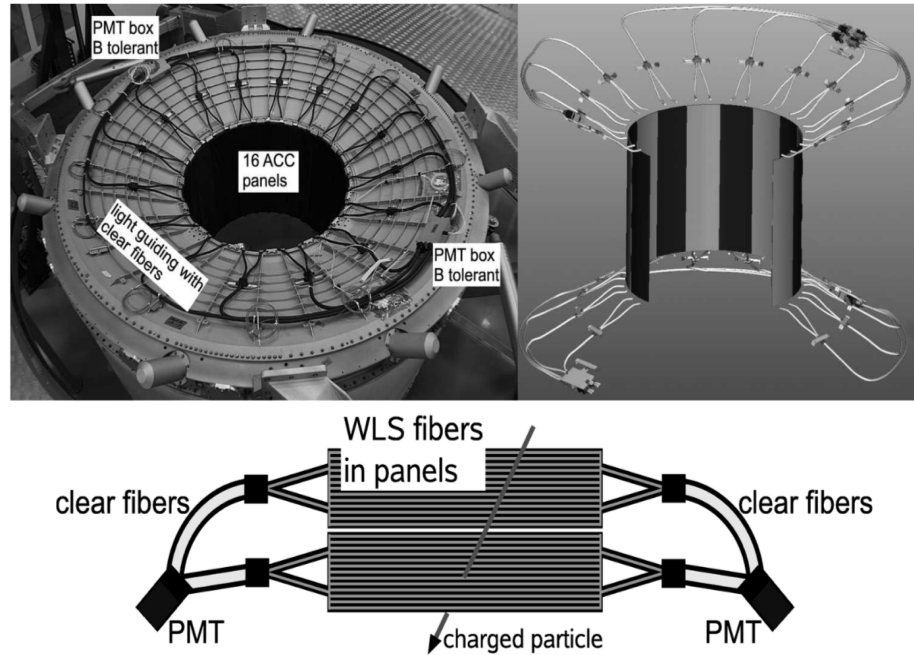


Figure 3.18: Upper left: ACC counter system. Upper right: the principle of ACC arrangement. Lower: Panel pair and PMTs connections. [87]